iScience

CellPress

Article

Spatiotemporally Controlled Myosin Relocalization and Internal Pressure Generate Sibling Cell Size Asymmetry

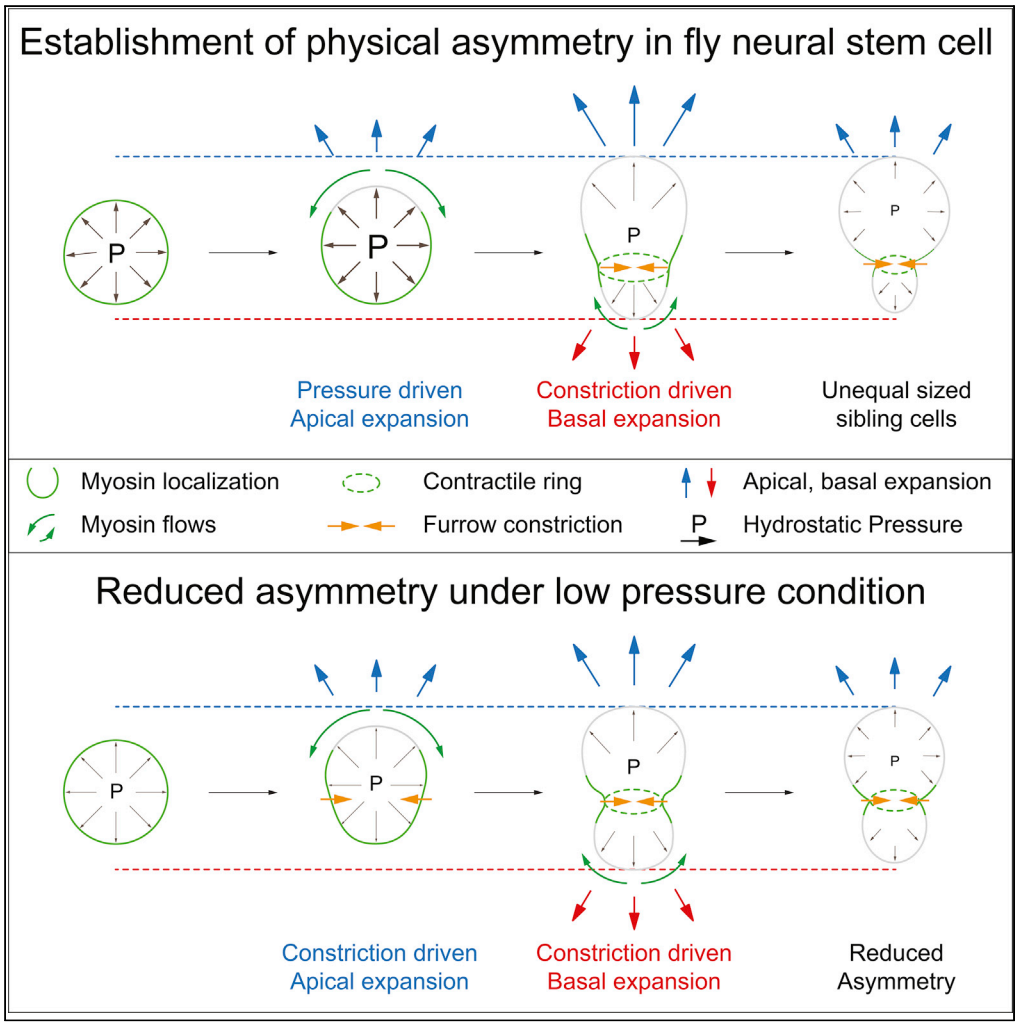

Tri Thanh Pham, Arnaud Monnard, Jonne Helenius, Erik Lund, Nicole Lee, Daniel J. Müller, Clemens Cabernard

ccabern@uw.edu

HIGHLIGHTS

Fly neural stem cells display stiffness asymmetry during mitosis

Hydrostatic pressure increases in fly neural stem cells before anaphase

Coordination of Myosin relocalization and pressure enables biased cortical expansion

Changes in hydrostatic pressure affect physical asymmetry

Pham et al., iScience *13*, 9–19
March 29, 2019
https://doi.org/10.1016/j.isci.2019.02.002

iScience

CellPress

Article

Spatiotemporally Controlled Myosin Relocalization and Internal Pressure Generate Sibling Cell Size Asymmetry

Tri Thanh Pham,[1] Arnaud Monnard,[1,2,6] Jonne Helenius,[3,6] Erik Lund,[1,5] Nicole Lee,[1,4] Daniel J. Müller,[3] and Clemens Cabernard[1,7,*]

SUMMARY

Metazoan cells can generate unequal-sized sibling cells during cell division. This form of asymmetric cell division depends on spindle geometry and Myosin distribution, but the underlying mechanics are unclear. Here, we use atomic force microscopy and live cell imaging to elucidate the biophysical forces involved in the establishment of physical asymmetry in *Drosophila* neural stem cells. We show that initial apical cortical expansion is driven by hydrostatic pressure, peaking shortly after anaphase onset, and enabled by a relief of actomyosin contractile tension on the apical cell cortex. An increase in contractile tension at the cleavage furrow combined with the relocalization of basally located Myosin initiates basal and sustains apical extension. We propose that spatiotemporally controlled actomyosin contractile tension and hydrostatic pressure enable biased cortical expansion to generate sibling cell size asymmetry. However, dynamic cleavage furrow repositioning can compensate for the lack of biased expansion to establish physical asymmetry.

INTRODUCTION

Sibling cell size asymmetry, here also called physical asymmetry, refers to the formation of unequally sized cells during cell division. Metazoan cells tightly regulate the mechanisms controlling symmetric or asymmetric physical cell divisions, but the mechanics and physiological roles are still unclear (Roubinet and Cabernard, 2014).

The anaphase spindle has been proposed to be the primary determinant for the positioning of the cleavage furrow (D'Avino et al., 2015; Rappaport, 1986; Glotzer, 2017; Green et al., 2011). Regulating spindle positioning, orientation, and geometry thus offers a mechanism for the generation of equal- or unequal-sized sibling cells (White and Glotzer, 2012; Roubinet et al., 2017; Albertson and Doe, 2003; Cai et al., 2003). For instance, changing spindle position or metaphase plate location of symmetrically dividing cultured human cells can induce physically asymmetric cell divisions (Kiyomitsu and Cheeseman, 2013; Tan et al., 2015). Flies and ascidians control spindle symmetry and positioning through microtubule-depolymerizing kinesin family proteins such as Klp10A or Kif2A (Costache et al., 2017; Derivery et al., 2015; Chen et al., 2016).

Drosophila neuroblasts, the neural stem cells of the developing central nervous system are an ideal system to investigate sibling cell size asymmetry. These cells divide asymmetrically by size and fate, forming a large self-renewed neuroblast and a small differentiating ganglion mother cell (GMC). Neuroblasts are intrinsically polarized (Homem and Knoblich, 2012; Gallaud et al., 2017), and changes in cell polarity affect spindle geometry and sibling cell size asymmetry (Albertson and Doe, 2003; Cabernard and Doe, 2009; Cai et al., 2003). However, findings from *Drosophila* and *C. elegans* neuroblasts suggest that cell size asymmetry is also regulated by asymmetric localization of non-muscle Myosin II (Myosin hereafter) (Cabernard et al., 2010; Connell et al., 2011; Ou et al., 2010). Fly neuroblasts relocalize Myosin to the cleavage furrow at anaphase onset through a basally directed cortical Myosin flow followed by, with a 1-min delay, an apically directed cortical Myosin flow. The molecular mechanisms triggering apical-basal cortical Myosin flow onset are not entirely clear but involve apically localized Partner of Inscuteable (Pins; LGN/AGS3 in vertebrates), Protein Kinase N, and potentially other neuroblast-intrinsic polarity cues. On the basal neuroblast cortex, spindle-dependent cues induce an apically directed cortical Myosin flow to the cleavage furrow. The

[1]Department of Biology, University of Washington, Life Science Building, Seattle, WA 98195, USA

[2]Biozentrum, University of Basel, Klingelbergstrasse 50-70, 4056 Basel, Switzerland

[3]Eidgenössische Technische Hochschule (ETH) Zurich, Department of Biosystems Science and Engineering, Mattenstrasse 26, 4058 Basel, Switzerland

[4]Cancer Science Institute, National University of Singapore, 14 Medical Dr., Singapore 117599, Singapore

[5]Present address: All4Cure, Cambia Grove, Seattle, WA 98101, USA

[6]These authors contributed equally

[7]Lead Contact

*Correspondence: ccabern@uw.edu

https://doi.org/10.1016/j.isci.2019.02.002

correct timing of these Myosin flows is instrumental in establishing biased Myosin localization and sibling cell size asymmetry in fly neuroblasts (Tsankova et al., 2017; Roth et al., 2015; Roubinet et al., 2017).

Spatiotemporally controlled Myosin relocalization provides a framework for the generation of unequal-sized sibling cells, but the forces driving biased cortical expansion are still unknown. Here, we use atomic force microscopy (AFM) to measure dynamic changes in cell stiffness and cell pressure (Krieg et al., 2018), combined with live cell imaging and genetic manipulations in asymmetrically dividing neuroblasts. We found that physical asymmetry is formed by two sequential events: (1) internal pressure initiates apical expansion, enabled by a Myosin-dependent softening of the apical neuroblast cortex and (2) actomyosin contractile tension at the basally shifted cleavage furrow subsequently initiates basal expansion while maintaining apical membrane expansion. Thus, spatiotemporally coordinated Myosin relocalization combined with hydrostatic pressure and cleavage furrow constriction enables biased membrane extension and the establishment of stereotypic sibling cell size asymmetry. Furthermore, we found that if biased cortical expansion is compromised, either by removing hydrostatic pressure or by altering spatiotemporally regulated Myosin relocalization, a dynamic adjustment of the cleavage furrow position compensates for the lack of biased expansion to rescue the establishment of physical asymmetry.

RESULTS

A Cell-Intrinsic Stiffness Asymmetry Precedes the Formation of the Cleavage Furrow

Cell shape changes are largely controlled by changes in mechanical stress and tension at the cell surface (Clark et al., 2015). During physical asymmetric cell division, cortical proteins are subject to precise spatiotemporal control (Roubinet et al., 2017; Tsankova et al., 2017), but how this impacts cell surface tension to allow for dynamic cell shape changes is incompletely understood (Figure 1A). To this end, we set out to measure cell stiffness—a measure of the resistance of the cell surface to an applied external force—of asymmetrically dividing larval brain neuroblasts with AFM. As *in vivo* these neural stem cells are surrounded by cortex glia apically, and GMCs and differentiating neurons basally, we established primary neuroblast cultures so that the AFM tip could directly probe the neuroblast surface. Cultured larval brain neuroblasts showed normal polarization and cell cycle timing (Figures S1A–S1C and Berger et al., 2012).

We used a rounded, 300-nm-radius AFM tip and measured neuroblast stiffness on ~20 positions along the apical-basal division axis every 30 s. The averaged measurements (n = 25 neuroblasts) were binned in five regions (apical, sub-apical, middle, sub-basal, and basal) (Figure 1B). Cell cycle stages and the position of measurement were determined using Sqh:GFP (Royou et al., 2002) (labeling Myosin's regulatory light chain) and GFP-tagged centrosomin (cnn:GFP, labeling centrosomes; Zhang and Megraw, 2007) (Figures S1D–S1H and Methods).

Our AFM measurements revealed that cell stiffness was mostly uniform before anaphase onset ranging from 0.5 to 0.8 nN μm^{-1}. At anaphase onset and 60 s thereafter ("0 s" marks anaphase onset in Figures 1C and 1D), we observed a noticeable increase in stiffness in the mid and sub-basal regions, reaching almost 1.0 nN μm^{-1}. Interestingly, this increase in stiffness appeared in the region of the prospective cleavage furrow, most likely coinciding with the localization of the centralspindlin component Tumbleweed (MgcRacGAP in vertebrates) (Roubinet et al., 2017). However, stiffness dropped over most of the cell cortex 90 s after anaphase onset, eliminating this apparent stiffness asymmetry. In late anaphase, stiffness increased again, predominantly in the cleavage furrow region. Taken together, these measurements revealed a stereotypic increase in neuroblast stiffness until anaphase onset before it dropped significantly thereafter. Furthermore, stiffness was not uniform but distributed asymmetrically in early anaphase and was at its highest in a basally shifted region corresponding to the prospective cleavage furrow.

Neuroblast Stiffness Is a Combination of Actomyosin Contractile Tension and Other Biophysical Parameters

Previously, it was suggested that cortical relaxation at the poles was responsible for biased membrane expansion during physical asymmetric cell division (Connell et al., 2011). Cortical relaxation could be induced through Myosin relocalization, prompting us to correlate stiffness changes with Myosin relocalization dynamics. As the wide-field imaging data were not sufficiently reliable to extract Myosin intensity we imaged third instar neuroblasts expressing Sqh:GFP with spinning disk microscopy and correlated the resulting intensity and curvature profiles with AFM stiffness data by calculating the relative change between

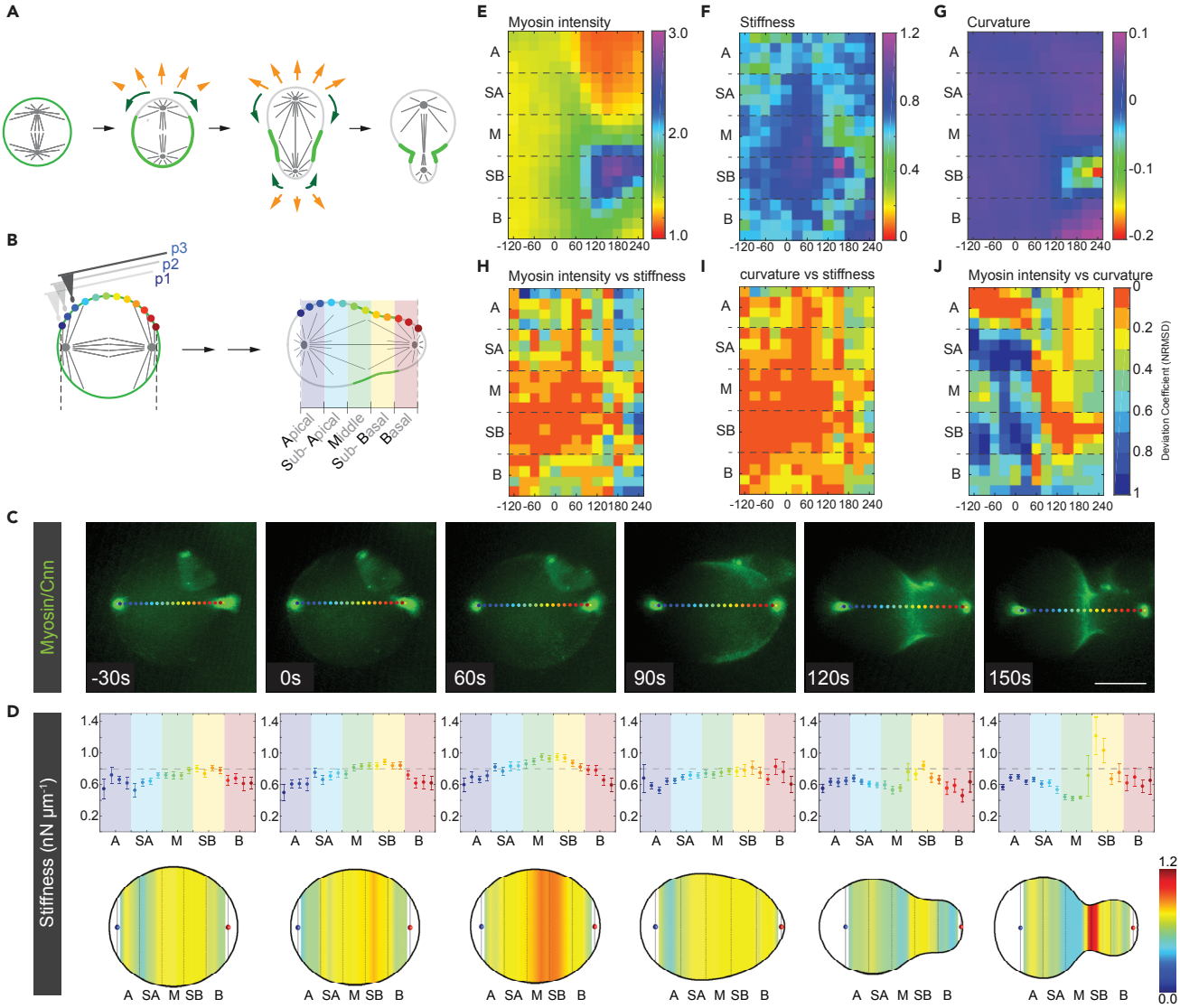

Figure 1. Cortical Stiffness Only Partially Correlates with Myosin Localization and Curvature

(A) Wild-type neuroblasts undergo biased membrane expansion (orange arrows) concomitant with spatiotemporally controlled Myosin relocalization (green arrows). Apical Myosin flows (green arrows) toward the cleavage furrow before the onset of an apically directed Myosin flow (green arrows).

(B) Schematic representation showing cortical stiffness measurement points along the cell cortex (colored circles) throughout mitosis. Measurements were binned into five cortical regions along the apical-basal neuroblast axis.

(C) Representative image sequence showing a wild-type neuroblast expressing Sqh:GFP (Myosin; green) and the centrosome marker Cnn:GFP (bright green dots) throughout mitosis. Positions where AFM measurements were performed are labeled with colored circles (see also Figure S1).

(D) Distribution of mean cortical stiffness and standard error of the mean (top row, n = 25) in all regions along the division axis throughout mitosis in reference to anaphase onset (0 s). The bottom row shows the corresponding heatmap for cortical stiffness.

(E–J) (E) Mean Myosin intensity (n = 19) at all sub-binned regions for wild-type neuroblasts; time axis is relative to anaphase onset. Mean stiffness (n = 25) and mean curvature (dimensional unit is μm^{-1}, n = 19) are shown in (F) and (G), respectively. Deviation coefficients (see Methods) were plotted to correlate Myosin intensity with cortical stiffness (H), curvature with stiffness (I), and Myosin intensity with curvature (J).

Scale bar, 5 µm.

Myosin intensity and cell curvature, and between Myosin intensity and cell stiffness. As reported previously (Roubinet et al., 2017), apical Myosin intensity started to decrease at anaphase onset, although stiffness increased again apically (Figures 1E and 1F). In the mid and sub-basal regions, both Myosin intensity and stiffness increased. Similarly, high Myosin intensity was visible at the forming cleavage furrow later in anaphase, concomitant with detectable changes in cell surface curvature. The most noticeable curvature changes became apparent in the furrow region from 120 s after anaphase onset onward (Figures 1E–1G).

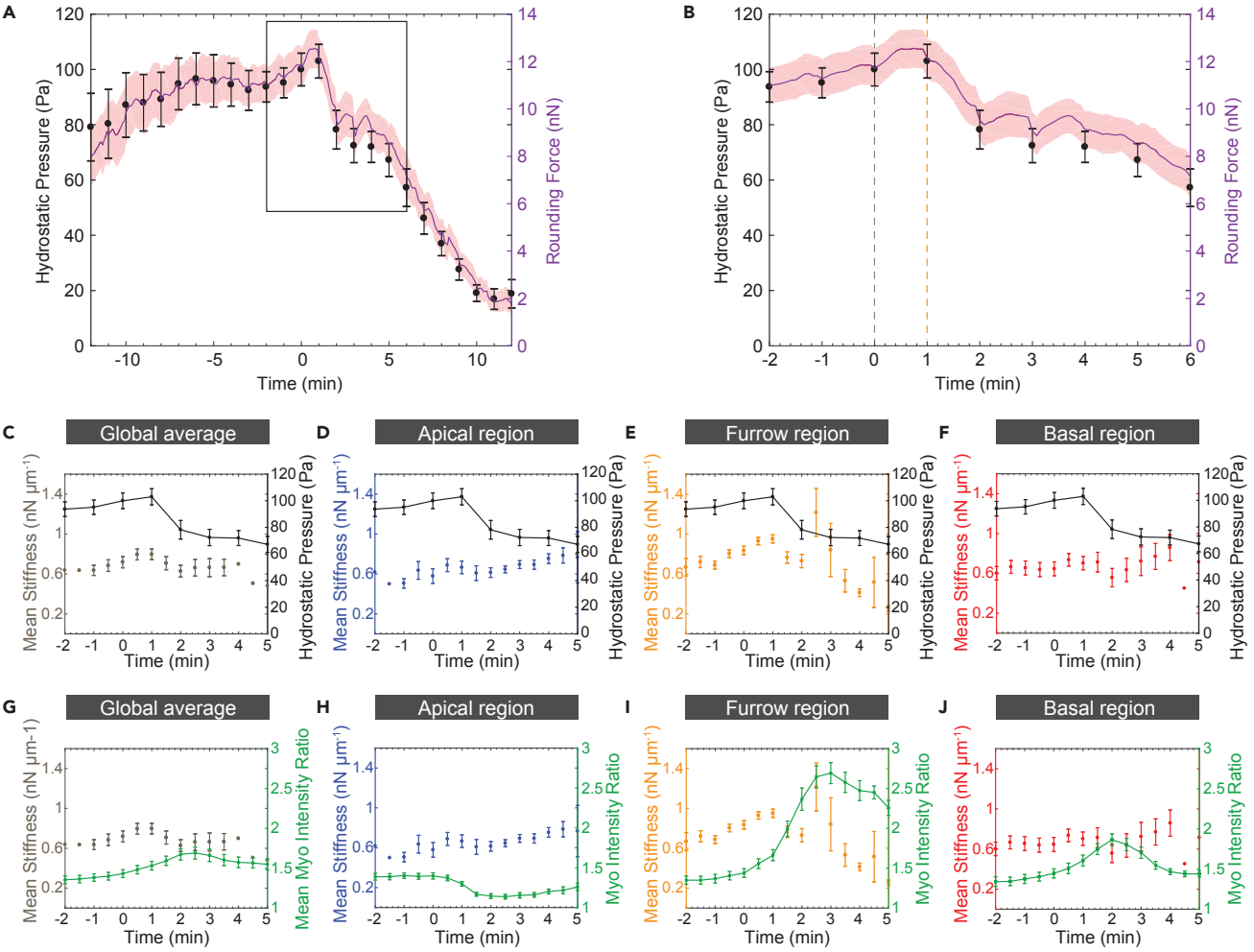

Figure 2. Hydrostatic Pressure Increases during Mitosis, Peaking Right after Anaphase Onset

(A–J) (A) Mean rounding force (magenta line) and mean hydrostatic pressure (black balls) measured by AFM using the parallel plate assay (see Figure S2 for more details; error bars represent standard error of the mean, n = 13) throughout mitosis for wild-type neuroblasts. The boxed measurements are shown enlarged in (B). The gray vertical line refers to anaphase onset (0 min). The orange vertical line highlights the onset of the hydrostatic pressure drop. Graphs showing the mean cortical stiffness and mean hydrostatic pressure throughout mitosis for (C) the entire neuroblast (global average) and the (D) apical, (E) furrow, and (F) basal regions. Graphs showing the mean cortical stiffness and mean Myosin intensity throughout mitosis for (G) the entire neuroblast (global average) and the (H) apical, (I) furrow, and (J) basal regions.

The resulting deviation coefficients revealed that Myosin intensity and curvature strongly correlate early (−120 to 30 s) on the apical neuroblast cortex and later in the cleavage furrow region (120 to 240 s); the shift in Myosin intensity from the apical cell cortex toward the furrow region, previously described as a cortical flow (Roubinet et al., 2017), was accompanied by a shift in curvature changes. Until 120 s after anaphase onset, stiffness correlated best with Myosin intensity in the cleavage furrow region. However, it is noticeable that Myosin intensity poorly correlated in many cortical regions with either curvature or stiffness (Figures 1H–1J and 2G–2J).

We conclude that asymmetrically dividing fly neuroblasts dynamically change stiffness locally, which only partially correlates with local Myosin accumulation and cell shape changes. We hypothesize that the local accumulation of Myosin filaments directly or indirectly affects cell surface properties in cortical regions with low Myosin filament concentration. For example, actomyosin constriction at the furrow can stretch the cortex in the apical region, which could result in a high stiffness value even in the absence of apical Myosin. Alternatively, the registered neuroblast stiffness could be a combination of Myosin activity and other biophysical parameters.

Neuroblasts Build up Hydrostatic Pressure until Anaphase Onset, Followed by a Pressure Drop in Early Anaphase

As cells increase their hydrostatic pressure during mitosis (Stewart et al., 2011), we wondered whether changes in neuroblast stiffness could be attributed to changes in hydrostatic pressure. We used a parallel plate assay to measure rounding force by pressing a wedge onto cultured neuroblasts expressing the membrane marker PH:GFP (see also Methods and Figure S2A). Rounding force gradually increased during mitosis before dropping sharply shortly after anaphase onset (Figure S2B). From these measurements, we used two methods to calculate the corresponding hydrostatic pressure. (1) We measured the surface area in contact with the AFM wedge for each time point and divided the registered rounding force by this value. (2) We used the Young-Laplace formula (Yoneda 1964, 1980) (see also Methods) to obtain the contact area before anaphase. At these stages, Young-Laplace calculations are very precise because cells are predominantly spherical before elongation in anaphase. However, because our contact area measurements were much higher than the calculated Young-Laplace surface area, probably due to optical aberrations, we calculated a correction factor and applied it to the detected contact area to extract hydrostatic pressure at all time points (Figures S2C and S2D). These measurements showed that cultured neuroblasts increase their intracellular hydrostatic pressure up to 105 Pa (Figures 2A and 2B; mean p = 103; SD = +/− 6.08; n = 13) 1 min after anaphase onset. However, 2 min after anaphase onset, hydrostatic pressure has already dropped by 20% compared with its peak value. Once division is completed, neuroblasts have a significantly lower hydrostatic pressure (mean p = 10.92; SD = ±3.72; n = 13) compared to the pressure at' the onset of mitosis.

Stiffness averaged over the entire neuroblast cortex followed hydrostatic pressure and also concomitantly increased at the apical, basal, and furrow regions. However, apical and basal stiffness poorly correlated with hydrostatic pressure from approximately 2 min after anaphase onset. Similarly, stiffness increased sharply in the cleavage furrow region 2.5 min after anaphase onset, whereas hydrostatic pressure had already dropped (Figures 2C–2F).

Taken together, these data suggest that at the cellular level, changes in hydrostatic pressure match neuroblast stiffness. However, on a subcellular level, local stiffness differs spatiotemporally from global hydrostatic pressure.

The Coordination between Hydrostatic Pressure and Myosin Relocalization Enables Biased Cortex Expansion

Next we asked how these dynamic changes in cell surface stiffness and hydrostatic pressure contribute to the establishment of sibling cell size asymmetry. Previously, we showed that Myosin relocalization dynamics strongly correlates with physical asymmetry (Roubinet et al., 2017; Tsankova et al., 2017; Connell et al., 2011), but the force underlying biased cortex expansion remained unexplained. Neuroblast cortex and membrane extension could be driven by (1) actomyosin contractile tension at the cleavage furrow (furrow constriction) displacing fluid and cytoplasmic material, (2) internal pressure, or (3) a combination of both (Figure 3A). We thus analyzed how dynamic changes in neuroblast pressure during mitosis correlate with Myosin relocalization, constriction, and biased cortical expansion. To this end, we imaged neuroblasts in intact brains, expressing Sqh:GFP and the spindle marker Cherry:-Jupiter, and quantified the extent of apical and basal cortical expansions in relation to anaphase onset and cleavage furrow ingression, constriction, and expansion rates, and Myosin intensity at the apical, basal, and furrow cortex (Figures 3B–3G, S3A, and S3B). Here, we consider furrow diameter reduction as the earliest sign of furrow constriction because it can be uncoupled from cortical extension (see below). We found that wild-type neuroblasts always started to expand shortly after anaphase onset on the apical neuroblast cortex first, followed by furrow diameter reduction. Expansion of the basal cell cortex occurred after furrow diameter reduction, almost at the same time as furrowing (furrow ingression) was detectable (Figure 3H). Before constriction, neuroblasts expanded by ~0.6 μm on the apical cortex, but no expansion was detected basally. Once constriction started, expansion was measureable on both the apical and basal neuroblast cortex (Figures 3I and 3J). These data suggest that (1) initial apical expansion is primarily driven by hydrostatic pressure and (2) sustained apical and all basal expansion is driven by furrow constriction. Furthermore, biased cortical expansion could correlate with Myosin relocalization dynamics. Indeed, apical expansion occurred shortly after anaphase onset, coinciding with a drop in apical Myosin intensity and high internal pressure. The onset of basal cortex expansion—~90 s after anaphase onset—coincided with decreasing levels of

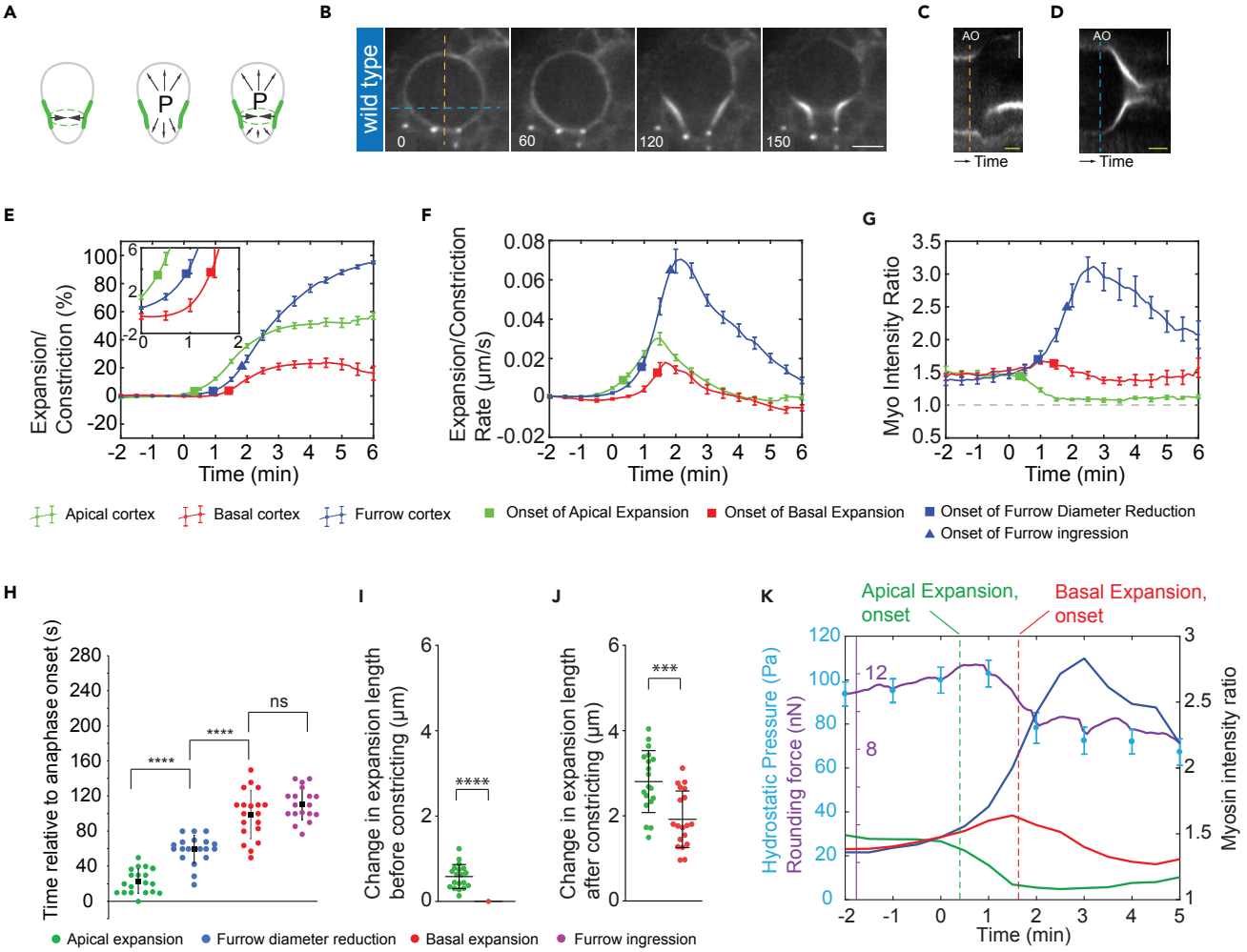

Figure 3. Internal Hydrostatic Pressure and Myosin Relocalization Dynamics Drive Asymmetric Cortical Expansion in Fly Neuroblasts

(A) Biased membrane expansion could be driven by furrow constriction, intracellular hydrostatic pressure, or a combination of both.

(B–G) (B) Representative image sequence showing a wild-type neuroblast expressing Sqh:GFP (white). Kymographs obtained along the apical-basal axis (orange dotted line) are shown in (C) or the furrow region (blue dotted line) in (D). Mean change in the expansion/constriction length (E), rate of change (F), and Myosin intensity (G) are plotted for the apical cortex (green), the basal cortex (red), and the furrow site (blue). Vertical bars refer to standard error of the mean (n = 19). The time axis is relative to anaphase onset (0 s). The inset in (E) shows a magnification of the 0- to 2-min time window.

(H–J) (H) Scatterplot showing the onset of apical expansion (green), onset of furrow diameter reduction (blue), onset of basal expansion (red), and onset of furrow initiation (when the curvature first changes from a straight line to an inward bending curve; purple). Changes in expansion length for both apical (green) and basal (red) cortex before and after furrow constriction (furrow diameter reduction) are shown in (I) and (J), respectively.

(K) Graph showing the mean rounding force (purple), mean hydrostatic pressure (cyan circles with error bars), mean Myosin intensity at the apical cortex (green), mean Myosin intensity at the basal cortex (red), and mean Myosin intensity at the furrow site cortex (blue). The green and red dashed lines represent the mean onsets of apical and basal expansions, respectively. Scale bar, 5 μm. Yellow timescale bar in kymographs, 2min.

Asterisks denote statistical significance, derived from unpaired t tests: ***p ≤ 0.001, ****p ≤ 0.0001; n.s., not significant.

basal Myosin, dropping hydrostatic pressure, and an increase in Myosin intensity at the cleavage furrow (Figure 3K).

We conclude that in wild-type neuroblasts, apical membrane expansion occurs when hydrostatic pressure is the highest. Basal cortical expansion coincides with an increase in Myosin at the cleavage furrow and a reduction of basally located Myosin. These data suggest that apical expansion is driven by high hydrostatic pressure and permitted by decreasing actomyosin contractile tension on the apical cortex. Basal membrane expansion, however, is primarily driven by an increase in cleavage furrow constriction and enabled by a lowering of actomyosin contractile tension on the basal cell cortex.

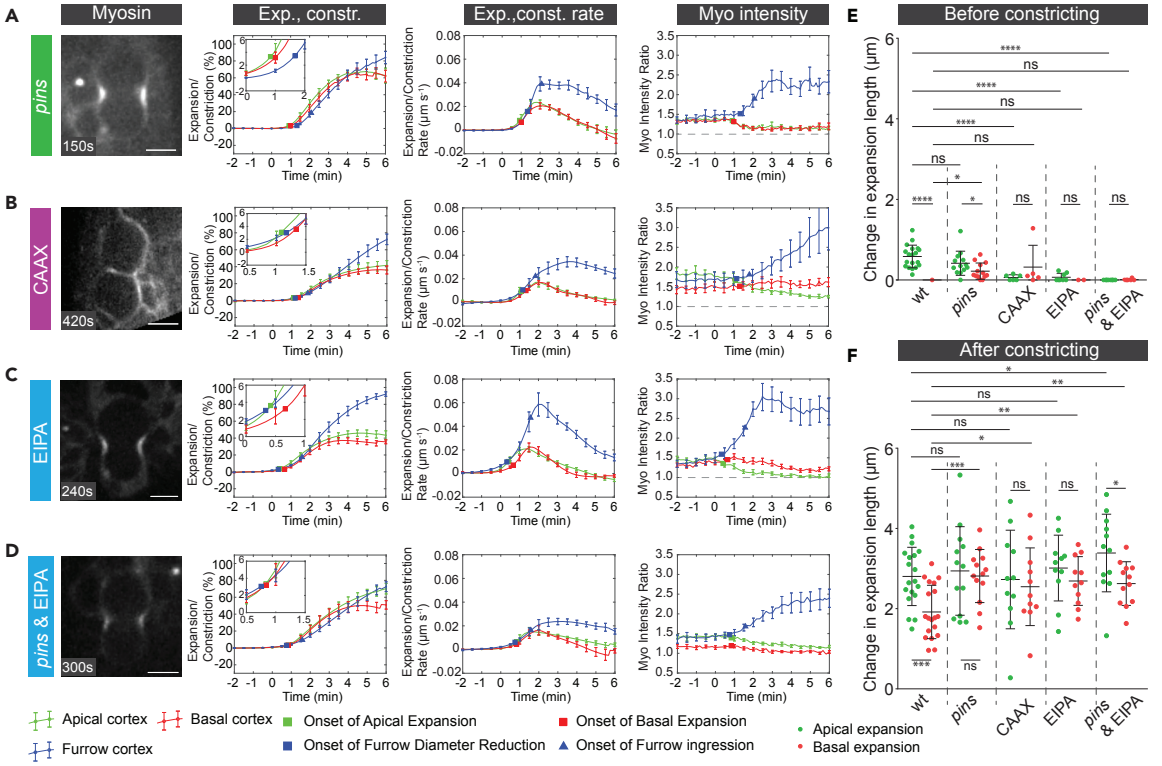
A
Myosin
Exp., constr.
Exp.,const. rate
Myo intensity
pins
150s
B
CAAX
420s
C
EIPA
240s
D
pins & EIPA
300s
Expansion/ Constriction (%)
Expansion/Constriction Rate (μm s⁻¹)
Myo Intensity Ratio
Time (min)
E
Before constricting
F
After constricting
Change in expansion length (μm)
wt
pins
CAAX
EIPA
pins & EIPA
Apical cortex
Basal cortex
Furrow cortex
Onset of Apical Expansion
Onset of Basal Expansion
Onset of Furrow Diameter Reduction
Onset of Furrow ingression
Apical expansion
Basal expansion
G
pins
H
CAAX
I
EIPA
J
pins & EIPA
Time relative to anaphase onset (s)
Apical expansion
Furrow diameter reduction
Basal expansion
K
Cell size ratio
L
Apical
Basal
ΔA
ΔB
ΔF
A
B
L
Ai
< 0
= 0
> 0
A = 0.5L + ΔA + ΔF
B = 0.5L + ΔB - ΔF
A - B = Ai
Ai = ΔA - ΔB + 2ΔF
M
(ΔA - ΔB)
Apical furrow shift
Basal furrow shift
Apical expansion
Basal expansion
ΔF
Asym
Sym
Inverted Asym
N
wt
pins
CAAX
EIPA
Cell size ratio (A/B)
R = 0.98
(ΔA-ΔB+2ΔF)/L
O
P
pressure, constriction
Time
Myosin localization
Myosin flows
contractile ring
Furrow constriction
Furrow shift
hydrostatic pressure
Apical, basal expansion

Figure 4. Physical Asymmetric Cell Division Is a Two-Step Process Driven by Internal Pressure and Spatiotemporally Controlled Myosin Relocalization

(A–J) Representative anaphase images, change in expansion/constriction length, expansion/constriction rate, and Myosin intensity shown for (A) *pins* (n = 13), (B) CAAX:vhhGFP4 expressing (n = 11), (C) EIPA-treated wild-type (n = 11), and (D) EIPA-treated *pins* mutant (n = 12) neuroblasts expressing Sqh:GFP (white). Measurements are shown for the apical cortex (green), the basal cortex (red), and the furrow site (blue). Time axis is relative to anaphase onset (0 s). Scatterplots showing the change in expansion length for the apical (green) and basal (red) cortex before (E) and after (F) constriction (furrow diameter reduction). Scatterplots showing the onset of apical expansion (green), furrow diameter reduction (blue), and basal expansion (red) for (G) *pins*, (H) CAAX:vhhGFP4-expressing, (I) EIPA-treated wild-type, and (J) EIPA-treated *pins* mutant neuroblasts.

(K) Scatterplots showing the cell size ratio for wild-type (n = 19), *pins* (n = 13), CAAX:vhhGFP4-expressing (n = 11), EIPA-treated wild-type (n = 11), and EIPA-treated *pins* mutant neuroblasts.

(L) Theoretical model describing the contribution of cortical expansion and furrow shift to daughter cell size difference (Ai, asymmetry index).

(M) Simulated heatmap defining different asymmetry regions based on the contribution of cortical expansion and the change in furrow positioning to the asymmetry index.

(N) Scatterplots showing the correlation between daughter cell size ratio and the normalized asymmetry index.

(O) Model. (1) Spatiotemporally regulated Myosin relocalization permits initial internal-pressure-driven apical expansion. (2, 3) Subsequently, owing to dissipation of internal pressure, sustained apical and subsequent basal expansion is driven by actomyosin-dependent furrow constriction. (3) Shifting or late positioning of the cleavage furrow can compensate for the lack of biased cortical expansion (see Figure S3 for more details).

See text for details. Scale bars, 5 μm. Asterisk denote statistical significance, derived from unpaired t tests: *$p \leq 0.05$, **$p \leq 0.01$, ***$p \leq 0.001$, ****$p \leq 0.0001$; n.s., not significant.

Spatiotemporal Control of Actomyosin Contraction Affects Expansion Dynamics and Sibling Cell Size Asymmetry

Next, we tested how global or local modulations in actomyosin contractile tension and changes in hydrostatic pressure affected biased cortical extension dynamics. We reasoned that relieving both the apical and basal cortices from actomyosin contractile cortical tension should permit hydrostatic pressure to drive symmetric expansion. To test this hypothesis, we analyzed *pins* mutant neuroblasts, which have been shown to clear Myosin from both the apical and basal cell cortex simultaneously (Cabernard et al., 2010; Tsankova et al., 2017; Roubinet et al., 2017). Indeed, in contrast to wild-type, apical and basal extension occurred to the same extent before furrow constriction in *pins* mutant neuroblasts (Figures 4A, 4G, 4E, 4F, S3C, and S3D). Similarly, delaying Myosin relocalization from both cell poles should prevent initial pressure-driven expansion and bias it toward constriction-driven expansion. To this end, we coexpressed Sqh:GFP together with the membrane-tethered nanobody ((pUAST-CAAX:vhhGFP4); vhhGFP4 has a high affinity for GFP; Saerens et al., 2005), thereby delaying Myosin relocalization on the apical and basal neuroblast cortex (referred to as CAAX hereafter). This manipulation abolished initial apical expansion, causing the apical and basal cell cortex to predominantly expand during furrow ingression (Figures 4B, 4H, 4E, 4F, S3E, and S3F).

Myosin relocalization dynamics can also be biased by removing the mitotic spindle using colcemid, a condition delaying basal Myosin relocalization while still permitting normal apical clearing (Roubinet et al., 2017; Roth et al., 2015). Although the lack of the mitotic spindle prevented us from determining anaphase onset, we found that expansion only occurred apically before constriction, followed by a late constriction-driven basal expansion event. As Myosin was retained basally, the basal cortex initially retracted, and we measured the extent of expansion following this initial retraction only (Figures S3G, S3H, and S3Q–S3S).

If hydrostatic pressure drives initial apical expansion, then lowering hydrostatic pressure should delay apical expansion until constriction sets in. In cells, hydrostatic pressure can be generated by an osmolarity gradient; if the osmolarity is higher inside the cell than outside, inflowing water will create hydrostatic pressure. Osmolarity and thus hydrostatic pressure can be changed by inhibiting ion transporters at the plasma membrane. We used ethylisopropylamiloride (EIPA), an inhibitor of Na^+/H^+ antiporters to reduce hydrostatic pressure (Stewart et al., 2011) in neuroblasts, and measured the subsequent expansion dynamics. EIPA did not affect Myosin dynamics, but wild-type or *pins* mutant neuroblasts exposed to EIPA predominantly abolished pre-constriction-driven expansion. Apical and basal expansion predominantly occurred after constriction started (Figures 4C–4F, 4I, 4J, and S3I–S3L).

Cell rounding is also regulated by a balance between actomyosin contractile tension and hydrostatic pressure (Stewart et al., 2011). Thus we hypothesized that lowering actomyosin contractile tension by reducing the amount of activated cortical Myosin should diminish intracellular hydrostatic pressure, thereby altering expansion dynamics. Adding the Rho kinase inhibitor Y-27632 to wild-type neuroblasts significantly

lowered cortical Myosin intensity; complete Rok inhibition showed no difference between cortical and cytoplasmic signals, whereas partial inhibition still contained lowered cortical Myosin levels (Figures S3M–S3P). Strong Rok inhibition prevented all apical and basal membrane extension and constriction (Figures S3M and S3N), but partial inhibition of Rok allowed apical and basal membranes to expand at the onset of furrow diameter reduction (Figures S3O and S3P). However, similar to EIPA-treated neuroblasts, most expansion occurred predominantly after furrow constriction set in (Figures S3Q–S3T). Thus lowering actomyosin contractile tension shifted the initial pressure-driven expansion toward constriction-driven expansion.

We conclude that Myosin localization and activity, as well as hydrostatic pressure, determine the cortical expansion dynamics. In the absence of hydrostatic pressure, or if actomyosin contractile tension is maintained, membrane expansion is primarily driven by cortical constriction. Furthermore, the spatiotemporal regulation of Myosin relocalization underlies biased cortical expansion dynamics.

Cleavage Furrow Shifting Can Compensate for the Lack of Biased Cortical Expansion

Finally, we tested how pressure-driven and constriction-driven expansions contribute to the establishment of physical asymmetry. In most cases, alterations in either cortical expansion dynamics by changing Myosin dynamics (*pins* mutants, CAAX neuroblasts), hydrostatic pressure (EIPA treatment), or both also affected sibling cell size asymmetry (Figures 4K and S3U). However, we noticed that some EIPA-treated and CAAX neuroblasts showed wild-type-like asymmetry ratios, although they expanded to the same extent on both the apical and basal cell cortex. We hypothesized that a shifting cleavage furrow could provide a mechanism to correct for the lack of expansion-driven physical asymmetry establishment. Indeed, EIPA-treated neuroblasts preferentially shifted the cleavage furrow toward the basal cortex, whereas wild-type neuroblasts can shift it in either direction (Figures S3V–S3X). We established a mathematical model that calculates an asymmetry index (Ai) as a measure of the degree of sibling cell size asymmetry (Figures 4L and 4M). This asymmetry index includes both polar cell expansion and cleavage furrow shift. For instance, in the absence of biased apical extension, wild-type-like physical asymmetry can be achieved by shifting the cleavage furrow basally. Alternatively, excessive basal expansion, combined with an apically shifted cleavage furrow, should result in inverted physical asymmetry (Figure 4M). To test this model, we measured apical and basal expansions as well as the cleavage furrow shift and found a good correlation with the final sibling cell size ratio (Figure 4N).

Taken together, we conclude that to establish physical asymmetry, shifting the cleavage furrow can compensate for the lack of biased cortical extension.

DISCUSSION

Sibling cell size asymmetry occurs in multiple cell types and organisms, but the underlying mechanisms are diverse and incompletely understood (Roubinet and Cabernard, 2014; Cabernard, 2017). Here, we characterized the biophysical forces underlying the formation of unequal sibling cell size in asymmetrically dividing fly neuroblasts. We used AFM to map dynamic changes in cellular stiffness throughout asymmetric cell division. These measurements revealed a characteristic stiffness asymmetry, marking the position of the prospective cleavage furrow already in early anaphase. This finding is consistent with our previous measurements, which revealed an accumulation of the centralspindlin component Tumbelweed in the prospective furrow region as well as an increase in actomyosin accumulation before measurable furrowing (Roubinet et al., 2017). Consistent with human cells (Stewart et al., 2011) we found that neuroblast stiffness increased during mitosis, peaking shortly after anaphase onset. The global increase in cell stiffness is predominantly attributed to an increase in intracellular pressure and only partially to local accumulation of Myosin. However, correlations between cellular stiffness and Myosin localization can be found at specific time points and cellular locations such as the cleavage furrow region in anaphase.

Here, we also report the interplay between Myosin relocalization, biased neuroblast cortex expansion, and changes in hydrostatic pressure, resulting in an intuitive model that can explain the establishment of sibling cell size asymmetry. Relieving the apical cell cortex from actomyosin contractile tension in early anaphase allows for pressure-driven biased cortical expansion. Subsequently, the drop in hydrostatic pressure—presumably due to an increase in cell volume—is compensated by an assembly of actomyosin at the cleavage furrow, which enables the continuation of apical extension and the onset of basal membrane extension

based on constriction-driven displacement of cytoplasmic material (Figure 4O). This biased cortical expansion is coordinated by actomyosin contractile tension, which underlies precise spatiotemporal control (Connell et al., 2011). For instance, apical Myosin relocalization dynamics is controlled by the apical polarity protein Pins through biased localization of Rok and Pkn (Cabernard et al., 2010; Tsankova et al., 2017) and basal Myosin relocalization is controlled by the spindle-dependent pathway (Roth et al., 2015; Roubinet et al., 2017). Both apical and basal Myosin relocalization occurs through cortical Myosin flow (Roubinet et al., 2017). Apical Myosin flow onset starts shortly after anaphase onset, at the peak of hydrostatic pressure. However, on the basal cell cortex, Myosin relocalization occurs with ~1-min delay (Roubinet et al., 2017), suggesting that the relaxing apical cell cortex permits initial pressure-driven apical expansion, but due to the delay of basal Myosin relocalization, reduced hydrostatic pressure is insufficient to overcome basal actomyosin contractile tension.

Biased cortical expansion is important to establish physical asymmetry. However, we discovered that neuroblasts utilize a backup mechanism to compensate for the lack of asymmetric polar expansion. For instance, modulating either hydrostatic pressure or Myosin distribution created situations in which both poles expand simultaneously. However, due to a shift in furrow positioning, or a late basal furrow positioning mechanism, these neuroblasts can still establish near wild-type-like physical asymmetry. Although we have not further investigated the mechanisms underlying final furrow positioning, previous results indicate that this is indirectly attributed to spindle-dependent cues (Cabernard et al., 2010; Roth et al., 2015; Roubinet et al., 2017). Spindle positioning, spindle geometry, or a combination thereof could influence the spatiotemporal establishment of a Myosin gradient. In wild-type neuroblasts, this gradient can be detected with our stiffness measurements and is already positioned early in anaphase. Modifications in spindle geometry and positioning could influence final furrow positioning by modulating Myosin flows. In sum, we propose that pressure-driven expansion, spindle geometry, and spindle positioning contribute toward the establishment of sibling cell size asymmetry. Under normal conditions, the primary determinant is biased cortical expansion, but if cortical expansion is compromised (either by reducing hydrostatic pressure or manipulating Myosin relocalization), a shifting furrow—most likely due to spindle geometry and/or positioning—can compensate.

Previously it was proposed that local modulations in cortical tension could allow cells to alter their shape (Stewart et al., 2011). Our study provides experimental evidence for this model under physiological conditions and could be potentially relevant to other invertebrate and vertebrate cells alike (Shin et al., 2013). In the future, it will be interesting to learn whether biased membrane extension is accompanied by asymmetric membrane addition or an unfolding of membrane stores. Similarly, the mechanisms regulating hydrostatic pressure during the cell cycle remain to be defined.

Limitations of the Study

The AFM data presented in this study are obtained from isolated neuroblasts. Our stiffness measurements thus neglect the contribution of neighboring cells such as cortex glia and GMCs. We also cannot exclude the possibility that the EIPA affects physiological processes other than hydrostatic pressure.

METHODS

All methods can be found in the accompanying Transparent Methods supplemental file.

SUPPLEMENTAL INFORMATION

Supplemental Information includes Transparent Methods, three figures, and one data and can be found with this article online at https://doi.org/10.1016/j.isci.2019.02.002.

ACKNOWLEDGMENTS

We thank members of the Cabernard laboratory for helpful discussions and Nicole Horsley for proofreading the manuscript. This work was supported by the Swiss National Science Foundation (SNSF; PP00P3_159318 to C.C. and 310030B_160255 to D.J.M.), the National Institutes of Health (NIH; 1R01GM126029-01, C.C.), and start-up funds from the University of Washington. T.T.P. was supported with a Systems X Transition Postdoc Fellowship (TPdF: SXFSIO_141991). Stocks obtained from the Bloomington Drosophila Stock Center (NIH P40OD018537) were used in this study.

AUTHOR CONTRIBUTIONS

This study was conceived by T.T.P. and C.C. T.T.P. performed all the experiments with help from A.M., E.L., N.L., and J.H. A.M. generated the CAAX:vhhGFP4 and PhyB:mcherry:CAAX constructs. Training and access to AFM microscopy was provided by J.H. and D.J.M. T.T.P. and C.C. wrote the paper.

DECLARATION OF INTERESTS

The authors declare no competing financial interests.

Received: May 22, 2018
Revised: November 12, 2018
Accepted: January 30, 2019
Published: March 29, 2019

REFERENCES

Albertson, R., and Doe, C.Q. (2003). Dlg, Scrib and Lgl regulate neuroblast cell size and mitotic spindle asymmetry. Nat. Cell Biol. *5*, 166–170.

Berger, C., Harzer, H., Burkard, T.R., Steinmann, J., van der Horst, S., Laurenson, A.S., Novatchkova, M., Reichert, H., Knoblich, J.A., et al. (2012). FACS purification and transcriptome analysis of Drosophila neural stem cells reveals a role for Klumpfuss in self-renewal. Cell Rep. *2*, 407–418.

Cabernard, C. (2017). Sibling cell size matters. Elife *6*, https://doi.org/10.7554/eLife.24038.

Cabernard, C., and Doe, C.Q. (2009). Apical/basal spindle orientation is required for neuroblast homeostasis and neuronal differentiation in Drosophila. Dev. Cell *17*, 134–141.

Cabernard, C., Prehoda, K.E., and Doe, C.Q. (2010). A spindle-independent cleavage furrow positioning pathway. Nature *467*, 91–94.

Cai, Y., Yu, F., Lin, S., Chia, W., Yang, X., et al. (2003). Apical complex genes control mitotic spindle geometry and relative size of daughter cells in Drosophila neuroblast and pI asymmetric divisions. Cell *112*, 51–62.

Chen, C., Inaba, M., Venkei, Z.G., Yamashita, Y.M., et al. (2016). Klp10A, a stem cell centrosome-enriched kinesin, balances asymmetries in Drosophila male germline stem cell division. Elife *5*, https://doi.org/10.7554/eLife.20977.

Clark, A.G., Wartlick, O., Salbreux, G., Paluch, E.K., et al. (2015). Stresses at the cell surface during animal cell morphogenesis. Curr. Biol. *24*, R484–R494.

Connell, M., Cabernard, C., Ricketson, D., Doe, C.Q., Prehoda, K.E., et al. (2011). Asymmetric cortical extension shifts cleavage furrow position in Drosophila neuroblasts. Mol. Biol. Cell *22*, 4220–4226.

Costache, V., Hebras, C., Pruliere, G., Besnardeau, L., Failla, M., Copley, R.R., Burgess, D., Chenevert, J., McDougall, A., et al. (2017). Kif2 localizes to a subdomain of cortical endoplasmic reticulum that drives asymmetric spindle position. Nat. Commun. *8*, 917.

D'Avino, P.P., Giansanti, M.G., Petronczki, M., et al. (2015). Cytokinesis in animal cells. Cold Spring Harb. Perspect. Biol. *7*, a015834.

Derivery, E., Seum, C., Daeden, A., Loubéry, S., Holtzer, L., Jülicher, F., Gonzalez-Gaitan, M., et al. (2015). Polarized endosome dynamics by spindle asymmetry during asymmetric cell division. Nature *528*, 280–285.

Gallaud, E., Pham, T., and Cabernard, C. (2017). *Drosophila melanogaster* neuroblasts: a model for asymmetric stem cell divisions. Results Probl. Cell Differ. *61*, 183–210.

Glotzer, M. (2017). Cytokinesis in metazoa and fungi. Cold Spring Harb. Perspect. Biol. *9*, a022343.

Green, R.A., Paluch, E., and Oegema, K. (2011). Cytokinesis in animal cells. Annu. Rev. Cell Dev. Biol. *28*, a015834.

Homem, C.C.F., and Knoblich, J.A. (2012). Drosophila neuroblasts: a model for stem cell biology. Development *139*, 4297–4310.

Kiyomitsu, T., and Cheeseman, I.M. (2013). Cortical dynein and asymmetric membrane elongation coordinately position the spindle in anaphase. Cell *154*, 391–402.

Krieg, M., Fläschner, G., Alsteens, D., Gaub, B.M., Roos, W.H., Wuite, G.J.L., Gaub, H.E., Gerber, C., Dufrêne, Y.F., and Muller, D.J. (2018). Atomic force microscopy-based mechanobiology. Nat. Rev. Phys. *475*, 1.

Ou, G., Stuurman, N., D'Ambrosio, M., Vale, R.D., et al. (2010). Polarized myosin produces unequal-size daughters during asymmetric cell division. Science *330*, 677–680.

Rappaport, R. (1986). Establishment of the mechanism of cytokinesis in animal cells. Int. Rev. Cytol. *105*, 245–281.

Roth, M., Roubinet, C., Iffländer, N., Ferrand, A., Cabernard, C., et al. (2015). Asymmetrically dividing Drosophila neuroblasts utilize two spatially and temporally independent cytokinesis pathways. Nat. Commun. *6*, 6551.

Roubinet, C., and Cabernard, C. (2014). Control of asymmetric cell division. Curr. Opin. Cell Biol. *31*, 84–91.

Roubinet, C., Tsankova, A., Pham, T.T., Monnard, A., Caussinus, E., Affolter, M., Cabernard, C., et al. (2017). Spatio-temporally separated cortical flows and spindle geometry establish physical asymmetry in fly neural stem cells. Nat. Commun. *8*, 1383.

Royou, A., Sullivan, W., and Karess, R. (2002). Cortical recruitment of nonmuscle myosin II in early syncytial Drosophila embryos: its role in nuclear axial expansion and its regulation by Cdc2 activity. J. Cell Biol. *158*, 127–137.

Saerens, D., Pellis, M., Loris, R., Pardon, E., Dumoulin, M., Matagne, A., Wyns, L., Muyldermans, S., Conrath, K., et al. (2005). Identification of a universal VHH framework to graft non-canonical antigen-binding loops of camel single-domain antibodies. J. Mol. Biol. *352*, 597–607.

Shin, J.-W., Buxboim, A., Spinler, K.R., Swift, J., Christian, D.A., Hunter, C.A., Léon, C., Gachet, C., Dingal, P.C., Ivanovska, I.L., et al. (2013). Contractile forces sustain and polarize hematopoiesis from stem and progenitor cells. Cell Stem Cell *14*, 81–93.

Stewart, M.P., Helenius, J., Toyoda, Y., Ramanathan, S.P., Muller, D.J., Hyman, A.A., et al. (2011). Hydrostatic pressure and the actomyosin cortex drive mitotic cell rounding. Nature *469*, 226–230.

Tan, C.H., Gasic, I., Huber-Reggi, S.P., Dudka, D., Barisic, M., Maiato, H., Meraldi, P., et al. (2015). The equatorial position of the metaphase plate ensures symmetric cell divisions. Elife *4*, https://doi.org/10.7554/eLife.05124.

Tsankova, A., Pham, T.T., Garcia, D.S., Otte, F., Cabernard, C., et al. (2017). Cell polarity regulates biased myosin activity and dynamics during asymmetric cell division via Drosophila rho kinase and protein kinase N. Dev. Cell *42*, 143–155.e5.

White, E.A., and Glotzer, M. (2012). Centralspindlin: at the heart of cytokinesis. In Cytoskeleton, *69*, D.N. Robinson, et al., eds. (Hoboken), pp. 882–892.

Yoneda, M. (1980). Tension at the highly stretched surface of sea-urchin eggs*. Dev. Growth Differ. *22*, 39–47.

Yoneda, M. (1964). Tension at the surface of sea-urchin egg: a critical examination of Cole's experiment. J. Exp. Biol. *41*, 893–906.

Zhang, J., and Megraw, T.L. (2007). Proper recruitment of -tubulin and D-TACC/Msps to embryonic drosophila centrosomes requires centrosomin motif 1. Mol. Biol. Cell *18*, 4037–4049.

ISCI, Volume *13*

Supplemental Information

Spatiotemporally Controlled Myosin Relocalization and Internal Pressure Generate Sibling Cell Size Asymmetry

Tri Thanh Pham, Arnaud Monnard, Jonne Helenius, Erik Lund, Nicole Lee, Daniel J. Müller, and Clemens Cabernard

Supplemental Figures

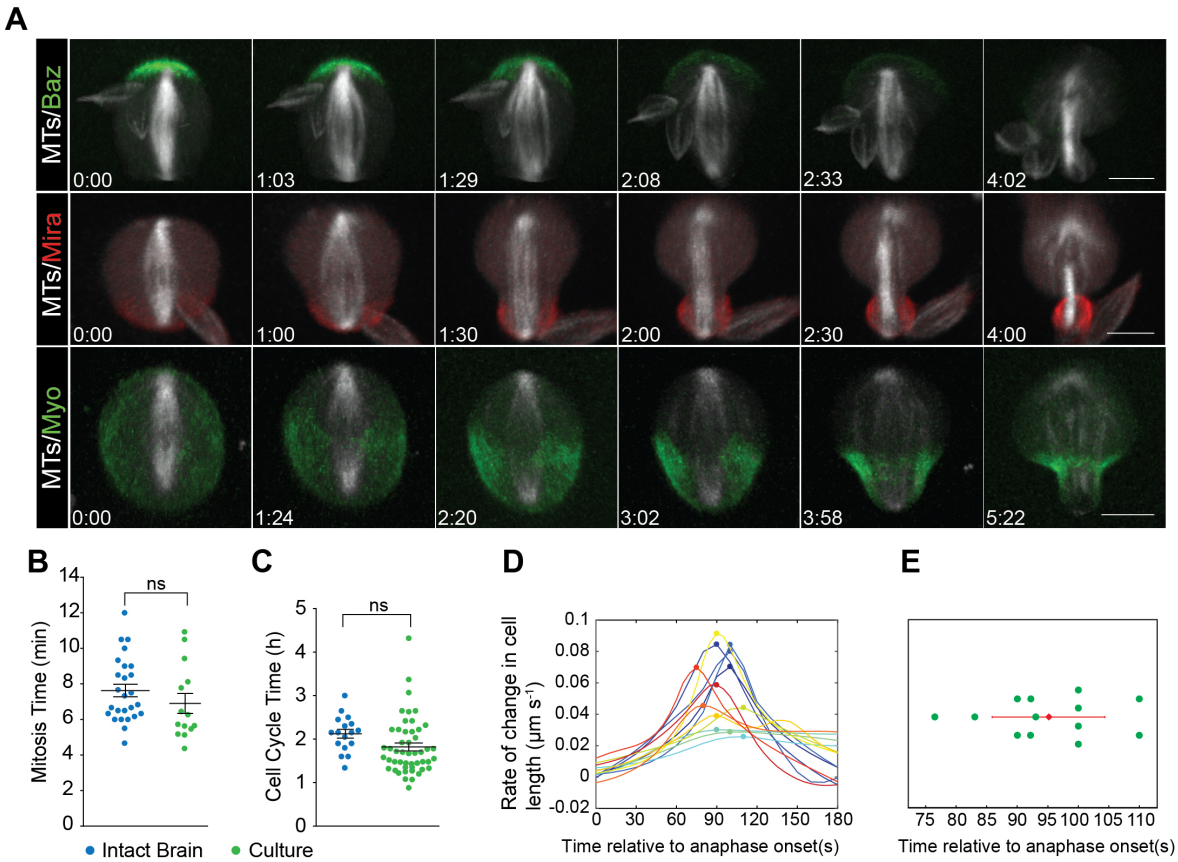

Figure S1. Cultured neuroblasts can be used to measure biophysical parameters, Related to Figure 1.

(A) Representative image sequence of a cultured wild type neuroblast expressing the apical polarity marker Baz::GFP (green; top row), the basal cell fate determinant Miranda (red; middle row) and the cell cortex marker Sqh::GFP (green; bottom row). All shown cells co-express the mitotic spindle marker pUAST-Cherry::Jupiter (white). Scatter plots showing **(B)** mitosis time and **(C)** the cell cycle time for cultured larval neuroblasts (green dots; n = 14 and 49) compared to larval neuroblasts in intact brains (blue dots; n = 26 and 17). **(D)** Graph showing the rate of change in cell length for several wild type neuroblasts in an intact brain (n=13). **(E)** Scatter plot showing the time when the peak rate of change in cell length occurs relative to anaphase onset. **(F)** Representative graph showing the raw AFM data for force versus indented height. Reliable cortical stiffness was extracted from the force vs indented height curve that fit well to a linear line for a portion of the raw data. **(G)** Representative graph showing how contact height was determined. **(H)** Schematic diagram showing how an AFM contact point can be projected onto the spindle axis to be sorted into regions for statistical averaging. Scale bar: 5 μm. Asterisk denote statistical significance, derived from unpaired t-tests: *; $p \leq 0.05$, **; $p \leq 0.01$, ***; $p \leq 0.001$, ****; $P \leq 0.0001$, n.s.; not significant.

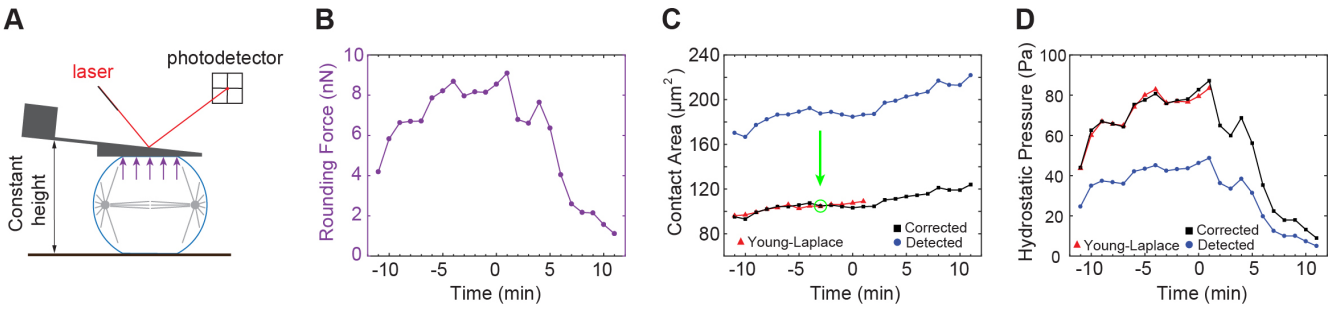

Figure S2. Rounding force increases during mitosis, peaking right after anaphase onset, Related to Figure 2.

(A) Schematic representation of a parallel plate assay (constant height assay) used to measure hydrostatic pressure throughout mitosis. **(B)** Rounding force detected by AFM throughout mitosis for a representative cell. The time axis is relative to anaphase onset (0 min). **(C)** Contact area was determined by two independent methods. (1) Theoretical contact area (red) calculated using the uniform tension model is very accurate, however it is only valid as long as cells are spherical. (2) Contact area detected by the total cell area that are in contact with the AFM wedge using fluorescent signal (blue). This method can be used at all cell cycle stages, but it tends to overestimate the contact area due to the point spread function of the imaging system. A correction factor (obtained at time point indicated by the green arrow) was applied to contact area measurements based on Young-Laplace calculations for spherical cells. **(D)** Hydrostatic pressure for the chosen representative cell was plotted per Young-Laplace (red), the detected contact area (blue) and the corrected contact area (black).

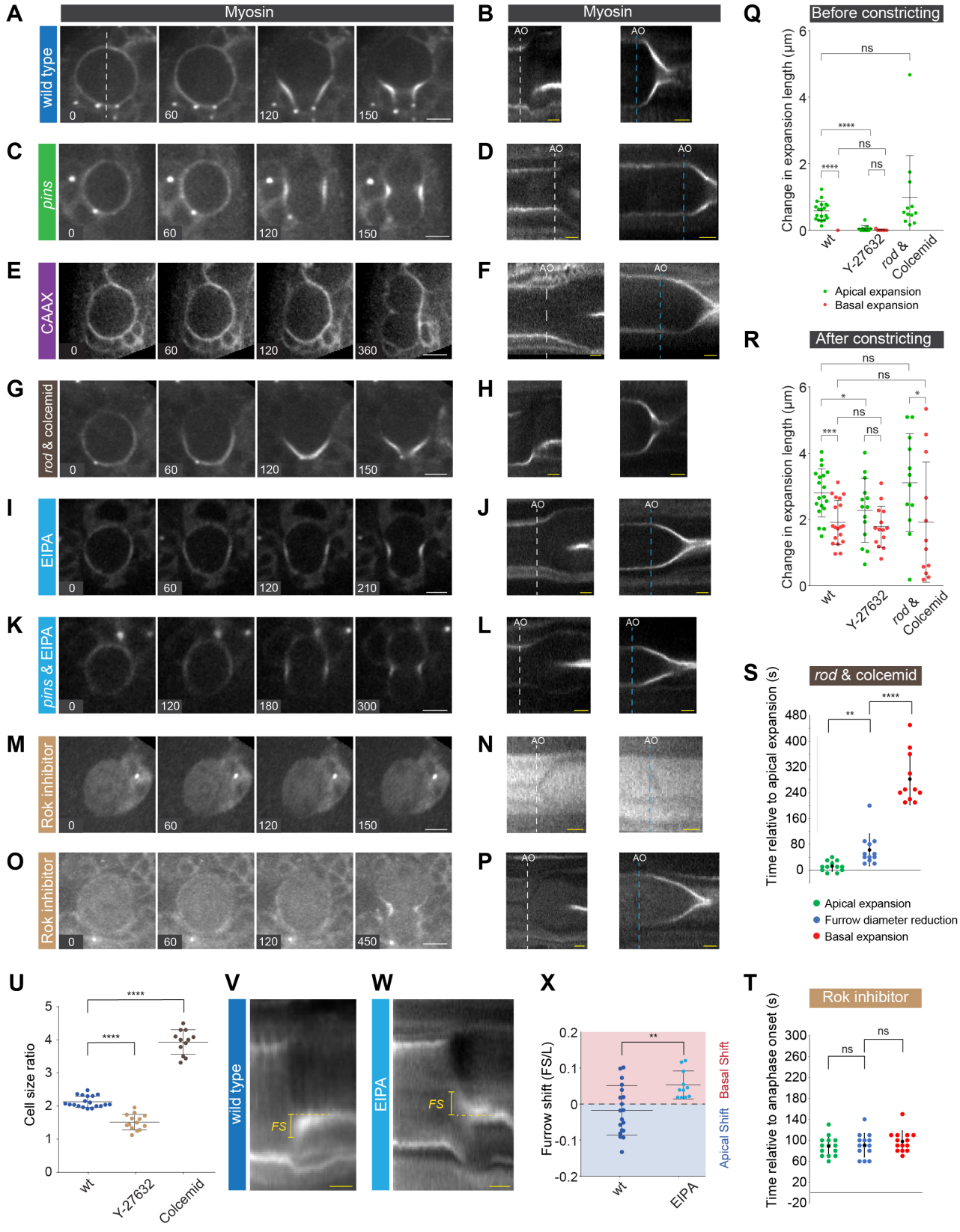
A
Myosin
wild type
0
60
120
150
B
Myosin
AO
C
pins
D
E
CAAX
360
F
G
rod & colcemid
H
I
EIPA
210
J
K
pins & EIPA
180
300
L
M
Rok inhibitor
N
O
450
P
Q
Before constricting
Change in expansion length (μm)
ns
****
wt
Y-27632
rod & Colcemid
Apical expansion
Basal expansion
R
After constricting
***
*
S
rod & colcemid
Time relative to apical expansion (s)
**
Furrow diameter reduction
T
Rok inhibitor
Time relative to anaphase onset (s)
U
Cell size ratio
Colcemid
V
FS
W
EIPA
X
Furrow shift (FS/L)
Basal Shift
Apical Shift

Figure S3. Myosin relocalization is essential for cortical expansion, Related to Figure 3&4.

Representative image sequences and kymographs obtained along the apical-basal axis and the furrow region of third instar neuroblasts expressing Sqh::GFP for **(A, B)** wild type, **(C, D)** *pins* mutant, **(E, F)** pUAST-CAAX::vhhGFP expressing wild type neuroblasts, **(G, H)** colcemid treated *rod* mutant neuroblasts, (**I, J**) EIPA treated wild type neuroblasts and (**K, L**) EIPA treated *pins* mutant neuroblasts and Y-27632 treated wild type neuroblasts resulting in complete **(M, N)** or partial **(O, P)** Rok inhibition. Change in expansion length for both apical (green) and basal (red) cortex before and after furrow constriction (furrow diameter reduction) for partial Y-27632 treated wild type neuroblasts (n=14) and colcemid treated *rod* mutant neuroblasts (n=12) are shown in (**Q**) and (**R**), respectively. (**S, T**) Scatter plot showing the onset of apical expansion (green), onset of furrow constriction (blue) and onset of basal expansion (red) for colcemid treated *rod* mutant neuroblasts (n=12) and Y-27632 treated wild type neuroblasts (n=14), respectively. (**U**) Scatter plot showing the sibling cell size ratio for Y-27632 treated wild type neuroblasts (n=14) and colcemid treated *rod* mutant neuroblasts (n=12), compared to wild type neuroblasts (n=19). Kymographs obtained along the apical-basal axis showing the dynamic change in furrow positioning for (**V**) wild type neuroblasts and **(W)** EIPA treated wild type neuroblasts. (**X**) Scatter plot showing the furrow shift during mitosis for wild type neuroblasts (n=19) and EIPA treated wild type neuroblasts (n=11). Time: seconds (s). Scale bar: 5 μm. Yellow time scale bar in kymographs: 2 min.

Transparent Methods

CONTACT FOR REAGENT AND RESOURCE SHARING

Further information and requests for resources and reagents should be directed to and will be fulfilled by the Lead Contact, Clemens Cabernard (ccabern@uw.edu).

EXPERIEMNTAL MODEL AND SUBJECT DETAILS

Fly strains and genetics

The following mutant alleles were used: *pins*^{P89} (Yu et al. 2000), *pins*^{P62} (Yu et al. 2000), *rod*$^{H4.8}$ (Basto et al. 2000), *sqh*^{AX3} (Jordan & Karess 1997).

Transgenes and fluorescent markers: *worGal4, pUAST-Cherry::Jupiter* (Cabernard & Doe 2009), *worGal4, pUAST-Cherry::Jupiter, Sqh::GFP* (Cabernard et al. 2010), *worGal4, pUAST-Cherry::Jupiter, pUAST-Mira::GFP* (Cabernard & Doe 2009), *Baz::GFP* (Buszczak et al. 2007), *Sqh::GFP* (Royou et al. 2002), *pUAST-Cnn::EGFP* (Megraw et al. 2002), *pUAST-pH::EGFP* (Bloomington stock center), *pUAST-attB-Caax::VhhGFP4* (this work), *pUAST-attB-PhyB::mcherry::CAAX* (this work).

Generation of transgenic lines

pUAST-attB-CAAX::VhhGFP4: The coding sequence of CAAX has been synthesized as oligonucleotides. VhhGFP4 (Saerens et al., 2005) was amplified by PCR (forward primer: AGGGAATTGGGAATTCCGCCACCATGGATCAAGTCCAACTGGTG; reverse primer: TCT TCTTTTTACGCGTGCTGGAGACGGTGACCTG) and cloned into the pUAST-attB vector using In-Fusion technology (Takara, Clontech). The resulting construct was injected into attP flies for targeted insertion on the third chromosome (VK00020, BestGene).

pUAST-attB-PhyB::mcherry::CAAX: The coding sequence of PhyB::mcherry::CAAX (Buckley et al., 2016) was amplified by PCR (Forward primer: GGGAATTGGGAATTC CGCCACCATGGTATCAGGTG;

Reverse primer: ACAAAGATCCTCTAGATTACATGAT AACACACTTGGTTTTTG) and cloned into the pUAST-attB vector using In-Fusion technology (Takara, Clontech). The resulting construct was injected into attP flies for targeted insertion on the third chromosome (VK00033, BestGene).

METHOD DETAILS

Colcemid, Y-27632 and EIPA experiments

For Y-27632 and colcemid and experiments, we used *worGal4, pUAST-Cherry::Jupiter, Sqh::GFP; pUAST-PhyB::mcherry::CAAX* and *worGal4, pUAST-Cherry::Jupiter, Sqh::GFP; rod$^{H4.8}$*, respectively. For EIPA (ethylisopropylamiloride) experiments, we used *pins^{P89}, pins^{P62}* and *worGal4, pUAST-Cherry::Jupiter, Sqh::GFP*. Dissected brains were incubated with Y-27632 (LC Labs) in live imaging medium at a final concentration of 62.5 μgmL^{-1}, with colcemid (Sigma) at a final concentration of 25 μgmL^{-1}, or with EIPA (Sigma) at a final concentration of 150 μM. Live imaging was acquired ~ 30 min after drugs addition. Complete spindle depolymerization was seen at the start of imaging for colcemid addition. Significant reduction of Sqh::EGFP on the neuroblast cortex was seen ~ 30 minutes after Y-27632 addition. Slight reduction in diameter of metaphase neuroblast was also observed ~ 30 minutes after EIPA addition.

Live cell imaging

Third instar larvae were used for all live cell imaging experiments. Live cell imaging was performed as described previously (Doe 2013) with the following minor modifications: S2 Media (Invitrogen) was supplemented with 10% HyClone Bovine Growth Serum (BGS, Thermo Scientific SH3054102). The larval brains were dissected in the supplemented S2 media and transferred into a μ-slide angiogenesis (ibidi). Live samples were imaged with an Andor revolution spinning disc confocal system, consisting of a Yokogawa CSU-X1 spinning disk unit and two Andor iXon3 DU-897-BV EMCCD cameras. A 60X/1.4NA oil immersion objective mounted on a Nikon Eclipse Ti microscope was used for most

images. Live imaging voxels sizes are 0.22 X 0.22 X 1µm (60x/1.4NA spinning disc).

sqh^{AX3}; worGal4, pUAST-Cherry::Jupiter, Sqh::GFP; pUAST-CAAX::VhhGFP4 larvae were kept at 18 °C and then incubated at 29°C up to 6h prior to imaging.

Image processing and measurements

Live cell imaging data was processed using Imaris x64 7.5.4 and ImageJ. Andor IQ2 files were converted into Imaris files using a custom-made Matlab code. Average intensity projections were generated in ImageJ. All Kymographs obtained from a line drawn from the apical to the basal cortex were generated with a 5-pixel wide. All Kymographs obtained from the furrow site were generated with a 9-pixel wide line. The intensity values at the apical, basal and furrow site, as well as in the cytoplasm were extracted using a custom-made Matlab code (Cortex position and intensity extract from kymograph analysis.m). For the intensity plots, the cortical intensities were normalized against the cytoplasmic values. The intensity at the cleavage furrow was obtained from an average value between the left and the right furrow cortex values. The curvature analysis was performed in ImageJ, using a custom made Matlab code (Cortex intensity and curvature extract from drawn boundary.m). Cortical intensities along the cell boundary were obtained from an average intensity of three pixels located perpendicular to the cell boundary.

Figures were assembled using Adobe Illustrator CS6 and all quantifications were performed in Matlab and Microsoft Excel.

Primary larval neuroblast culture procedure

Primary neuroblast cultures were prepared as previously reported (Berger et al. 2012). In brief, wild type brains were dissected in Chan and Gehring's medium and incubated with Collagenase Type I (Sigma) and Papain (Sigma) at 30° C for 30 min at a final concentration of 1mg/mL. The brains were gently washed twice with 400 µL of supplemented Schneider's medium. The brains were then placed in a 1.5

mL tube with 200 µL of supplemented Schneider's medium and homogenized using a 200 µL pipette tip by pipetting several times until the solution looked homogenous.

AFM measurements

All stiffness measurements were performed using a Nanowizard II JPK AFM (JPK Instruments, Germany), coupled with an inverted optical microscope (Zeiss Axiovert 200, Germany). All experiments were performed in solution using intermittent contact. In order to measure cortical stiffness, isolated wild type neuroblasts expressing Sqh::EGFP and Cnn::EGFP were plated on a cover-glass bottom dish (FluoroDish, WPI, INC., Sarasota, FL, USA). The cover-glass bottom disc was coated with 10 µg mL^{-1} of Concanavalin A to anchor the cell to the glass surface and prevent slippage when pressing the cell with the AFM tip. The sample was placed on the AFM stage mounted on top of the optical microscope. A Plan Apochromat 63X/1.4NA oil immersion objective was used together with the Zeiss AxioCam MRm monochrome digital camera to sequentially acquire fluorescent images with cortical stiffness measurements. Live imaging voxels sizes are 0.0993 X 0.0993 X 1 µm (63x/1.4NA). High aspect ratio bead tipped cantilevers with a nominal spring constant of 0.2 N m^{-1} and a tip height in the range of 10-15 µm with a spherical 300 nm radius (B300_CONTR, Nanoandmore, Germany) were employed. A force-volume line scan consisting of 30 equally spaced measurement points along a 20 µm line was used to probe local cortical stiffness with a maximal applied force of 0.6 nN. The extension velocity and the extension length were set at 20 µm s^{-1} and 8 µm, respectively. Each image stack and the subsequent line scan took approximately 30 s to complete. Unreliable AFM measurements, visible in the force curves, were excluded from the analysis (Figure S1F,G).

To determine the neuroblast's mitotic stage we used Cnn::GFP to measure the distance between centrosomes at all measured time points and plotted the cell elongation rates, which usually peaked at around 90 s after anaphase onset. This provided a measurement for determining the mitotic stage with ~ 30 s accuracy (Figure S1D,E).

QUANTIFICATION AND STATISTICAL ANALYSIS

Curvature analysis

To determine the local curvature along the cell cortex, a line was manually drawn in ImageJ from the apical to the basal cortex on the mid-plane. Local cortical curvature *K* can be determined via the following formula: $K = \frac{f''(x)}{(1+f'^2(x))^{3/2}}$, where x and $f(x)$ are the horizontal and vertical position of the drawn cortex, respectively. The first and second derivatives ($f'(x)$ and$f''(x)$) of the curve were calculated numerically using second order difference methods. Custom-written Matlab codes (Cortex intensity and curvature extract from drawn boundary.m) were used to determine curvature values for all points on the curve.

Kymograph quantification

Cell mid-planes were first generated using the Oblique Slicer tool in Imaris (Bitplane) and the entire image volume was then resliced along the direction of this plane for all time points. Using ImageJ, an average intensity projection was generated from three selected planes closest to the mid-plane. This procedure was done for all acquired time points. Kymographs were then generated by drawing a five pixel wide straight line from the apical to the basal cortex for all time points. To determine cortical intensity signal from a kymograph, a spline curve was drawn along the cortex on the kymograph and the XY coordinates of this curve were exported to a text file. Custom made Matlab codes (Cortex position and intensity extract from kymograph analysis.m) were written to extract the exact XY coordinates of the drawn curve from the text file without any repetitive time points by using a standard interpolation method. Intensity signal of the drawn curve was calculated from the grayscale kymograph image using an average intensity of the three pixels, closest to the curve.

Onset of expansion/constriction quantifications

The position of the apical, basal and furrow site cortices were traced by drawing a spline curve along each of these boundaries using the Kymographs generated earlier. The onset of expansion was chosen at the time point when the cortex expands to 3% of the cell metaphase radius (i.e. radius at 30 s before anaphase onset was used in this case). The onset of constriction was set in a similar manner. This 3% change in radius value was chosen because it is equivalent to a one pixel change on the image obtained from the 60X objective, which can also be detected by eye.

Cortical stiffness quantifications

Cortical stiffness is obtained from the slope of the linear part of the force-depth curve. Data with a force range from 60% to 100% of the maximal force was used to fit a linear regression curve (Figure S1). To determine the reliability of the cortical stiffness extracted from the fitted line, the mean square error of the fit was used. The extracted cortical stiffness is classified as a reliable measurement when the mean square error of the fit is lower than the mean peak-peak fluctuation of the system, which is ~0.015 nN. Only reliable measurements were used to determine statistical average for each local region along the cell.

To determine the location of the AFM measurement points relative to the cell spindle-axis, precise location of the cell centrosomes and the contact point where the AFM tip touches the cell's surface is required. The contact height for any measurement point was determined from the point along the force vs indentation height curve that fit the curve best with two linear lines. The position of each centrosome was obtained from the xyz location of a spot placed at the highest intensity signal of the centrosomal marker Cnn::EGFP. The xy position of all AFM measurement points were determined by recording the first and the last position of the AFM tip. The centrosome height and the AFM contact height were synchronized using the cell mid-plane at metaphase as the reference height. The location of the cortical stiffness measurement relative to the spindle axis between the two centrosomes was determined using vector projections. At any cell cycle stage, the distance between the two centrosomes was binned into

20 equally distributed regions and reliable cortical stiffness measurements were accumulated for statistical average.

Pressure quantifications

Isolated wild type neuroblasts expressing pUAST-Cherry::Jupiter and pUAST-PH::EGFP were plated on a WPI glass bottom disc without any coating. The sample was placed on a JPK Cellhesion 200 stage which was mounted on top of a Zeiss confocal microscope (LSM 700). A custom-made flat PDMS wedge tip was held constantly at 5 µm above the glass bottom surface above the neuroblast. As the neuroblast enters mitosis, it rounds up and exerts a force on the wedge AFM tip, which can be detected by the photodetector. A Plan Apochromat 63X/1.4NA oil immersion objective was used to simultaneously image the neuroblast every minute while recording the exerted force. Hydrostatic pressure can be determined by taking the ratio of the detected forces and the area that was in contacted with the wedge (Stewart et al. 2013).

Correlation plots

To determine the correlation between any two quantities of interest which were acquired independently, a normalized root-mean-square deviation method (Maiorov & Crippen 1994) was used, hereby defined as the deviation coefficient. To obtain the deviation coefficient for all regions at a particular time point, the two curves were first normalized before the absolute difference was calculated. The deviation coefficients for all time point throughout mitosis was accumulated and normalized to their maximum value (NRMSD). A low deviation coefficient indicates a high correlation.

Definition of statistical tests, sample number, sample collection, replicates.

Analyses were performed with MATLAB and Graphpad Prism. For each experiment, the data was collected from at least 3 independent experiments. For each independent experiment, at least 5 larvae

were dissected. Statistical significance was determined using two-sample equal or unequal variance *t*-tests. Significance was indicated as following: *; $p < 0.05$, **; $p < 0.01$, ***; $p < 0.001$, ****; $p < 0.0001$. ns; not significant.

DATA AND SOFTWARE AVAILABILITY

MATLAB codes

AndorIQ to Imaris merge autosave.m: This code first imports the primary channel of Andor IQ raw data into Imaris and then adds the slave channel of Andor IQ raw data into Imaris as a second channel. The file was automatically saved once both channels were successfully loaded into Imaris.

AFM reliability analysis.m: This code imports the raw data recorded from the AFM experiments and extracts cortical stiffness and contact height. The reliability of cortical stiffness was characterized by how well the linear region of the force curve fit to a straight-line compared to the mean peak-to-peak fluctuation of the system.

AFM region statistics.m: This code reads the coordinates of the centrosomes as well as the calculated cortical stiffness and contact height from the text files to determine the position of the measurement points relative to the spindle axis. The cell mid-plane at metaphase was used as a reference height for both the centrosomes and the AFM measurement points. The data was binned into 20 equal regions along the spindle axis and accumulated from all measured cells to determine statistical averages.

Cortex position and intensity extract from kymograph analysis.m: This code reads the Kymograph .tiff image and the coordinate .txt files which recorded the position of the apical and basal cortex, and the cytoplasm for each time point on the kymograph. Since ImageJ automatically interpolated the

position coordinates from a drawn line, the coordinate .txt file contains more time points than present. This code filters out the repeated time points and calculates the average intensity at each position for all time points.

Cortex intensity and curvature extract from drawn boundary.m: This code reads the coordinates of the cell cortex boundary from the text files to determine the curvature and Myosin intensity at each pixel position on the cell cortex along the apical-basal division axis.

Deviation coefficient analysis.m: This code calculates the root-mean-square difference between any two quantities and normalizes the outcome to the absolute maximum value, generating the deviation coefficient for all regions and time points provided.

Rounding force extract at each imaging time point.m: This code extracts the rounding force at recorded time point to calculate the hydrostatic pressure.

Pressure calculation using theoretical contact area.m: This code detects the cell boundary and calculates the area inside the cell for each slice to determine the mid-plane slice with the largest cross section. Theoretical contact area was calculated using the best fitted radius for the mid-plane slice and the cell height under the AFM cantilever. Hydrostatic pressure was determined by taking the ratio of rounding force to the contact area.

Pressure calculation using detected contact area.m: This code reads the coordinate.txt file which contains the position of the outer boundary of the contact surface where the cell is in contact with the

AFM wedge. Hydrostatic pressure was determined by calculating the ratio between the rounding force and the detected contact area.

Pressure calculation using correction factor.m: This code calculates the ratio between the detected contact area and the theoretical contact area at a cell cycle stage when the cell mid-plane boundary fits the circle best. This ratio was used as a correction factor and applied to all the detected contact areas. The resulting product is the corrected contact area, which was used to determine the corrected hydrostatic pressure for all time points throughout mitosis.

KEY RESOURCES TABLE

REAGENT or RESOURCE	SOURCE	IDENTIFIER
Biological Samples		
Larval brain tissues from wild type and mutant *Drosophila melanogaster* strains	This study	N/A
Chemicals, Peptides, and Recombinant Proteins		
Bovine Growth Serum	Thermo Scientific	Cat# SH3054102
Schneider's Insect Medium	Sigma-Aldrich	Cat# S0146
Colcemid (MT inhibitor)	Sigma-Aldrich	Cat# D7385
Rho kinase inhibitor Y-27632	LClabs	Cat# Y-5301
5-(N-Ethyl-N-isopropyl)amiloride (EIPA)	Sigma-Aldrich	Cat# A3085
Collagenase Type I	Sigma-Aldrich	Cat# C0130
Papain	Sigma-Aldrich	Cat# P4762
Chan and Gehring's medium	(Chan & Gehring 1971)	
Experimental Models: Organisms/strains		
D. melanogaster: $pins^{P89}$	(Yu et al. 2000)	FBal0104444
D. melanogaster: $pins^{P62}$	(Yu et al. 2000)	FBal0104445
D. melanogaster: $rod^{H4.8}$	(Basto et al. 2000)	FBal0014638
D. melanogaster: Sqh^{AX3}	(Jordan & Karess 1997)	FBal0035707
D. melanogaster: *worGal4, UAS-Cherry::Jupiter*	(Cabernard & Doe 2009)	FBtp0040573
D. melanogaster: *worGal4, UAS-Cherry::Jupiter, Sqh::GFP*	(Cabernard et al. 2010)	FBtp0040573
D. melanogaster: *Baz::GFP*	(Buszczak et al. 2007)	
D. melanogaster: *worGal4, UAS-Cherry::Jupiter; Mira::GFP*	(Cabernard & Doe 2009)	FBtp0041413
D. melanogaster: *Sqh::GFP*	(Martin et al. 2009)	FBrf0151365
D. melanogaster: *UAS-Cnn::EGFP*	(Megraw et al. 2002)	FBrf0152123
D. melanogaster: *UAS-pH::EGFP*	Bloomington	BDSC:39693
D. melanogaster: *pUAST-attP-PhyB::mCherry::CAAX*	This paper	
D. melanogaster: *pUAST-attP-CAAX::VhhGFP4*	This paper	
Oligonucleotides		
Forward primer for *pUAST-attP-CAAX::VhhGFP4* AGGGAATTGGGAATTCCGCCACCATGGATCAAGTCCAACTGGTG	This paper	
Reverse primer for *pUAST-attP-CAAX::VhhGFP4* TCTTCTTTTTACGCGTGCTGGAGACGGTGACCTG	This paper	

Forward primer for *pUAST-attP-PhyB::mCherry::CAAX* GGGAATTGGGAATTCCGCCACCATGGTATCAGGTG	This paper	
Reverse primer for *pUAST-attP-PhyB::mCherry::CAAX* ACAAAGATCCTCTAGATTACATGATAACACACTTGGTTTTTG	This paper	
Recombinant DNA		
pUAST-attB-CAAX::VhhGFP4	This paper	
pUAST-attB-PhyB::mCherry::CAAX	This paper	
Software and Algorithms		
ImageJ	N/A	https://imagej.nih.gov/ij/
Imaris 7.6.4	Bitplane	http://www.bitplane.com/imaris
MATLAB	Mathworks	https://www.mathworks.com
Prism	GraphPad	https://www.graphpad.com
Matlab code to calculate curvature values	This paper	
Matlab code to calculate deviation coefficients	This paper	
Matlab code to extract rounding forces	This paper	
Matlab code to calculate theoretical pressure	This paper	
Matlab code to calculate detected pressure	This paper	
Matlab code to corrected pressure	This paper	
Matlab code to convert raw imaging data files into Imaris (Bitplane) file format	This paper	

Supplemental References

Basto, R., Gomes, R. & Karess, R.E., 2000. Rough deal and Zw10 are required for the metaphase checkpoint in Drosophila. *Nature cell biology*, 2(12), pp.939–943.

Berger, C. et al., 2012. FACS Purification and Transcriptome Analysis of Drosophila Neural Stem Cells Reveals a Role for Klumpfuss in Self-Renewal. *Cell reports*, 2(2), pp.407–418.

Buszczak, M. et al., 2007. The carnegie protein trap library: a versatile tool for Drosophila developmental studies. *Genetics*, 175(3), pp.1505–1531.

Cabernard, C. & Doe, C.Q., 2009. Apical/basal spindle orientation is required for neuroblast homeostasis and neuronal differentiation in Drosophila. *Developmental cell*, 17(1), pp.134–141.

Cabernard, C., Prehoda, K.E. & Doe, C.Q., 2010. A spindle-independent cleavage furrow positioning pathway. *Nature*, 467(7311), pp.91–94.

Chan, L.N. & Gehring, W., 1971. Determination of blastoderm cells in Drosophila melanogaster. *Proceedings of the National Academy of Sciences*, 68(9), pp.2217–2221.

Doe, C.Q., 2013. Live imaging of neuroblast lineages within intact larval brains in Drosophila. *Cold Spring Harbor Protocols*, 2013(10), pp.970–977.

Jordan, P. & Karess, R., 1997. Myosin light chain-activating phosphorylation sites are required for oogenesis in Drosophila. *The Journal of cell biology*, 139(7), pp.1805–1819.

Maiorov, V.N. & Crippen, G.M., 1994. Significance of root-mean-square deviation in comparing three-dimensional structures of globular proteins. *Journal of molecular biology*, 235(2), pp.625–634.

Martin, A.C., Kaschube, M. & Wieschaus, E.F., 2009. Pulsed contractions of an actin-myosin network drive apical constriction. *Nature*, 457(7228), pp.495–499.

Megraw, T.L. et al., 2002. The centrosome is a dynamic structure that ejects PCM flares. *Journal of cell science*, 115(Pt 23), pp.4707–4718.

Royou, A., Sullivan, W. & Karess, R., 2002. Cortical recruitment of nonmuscle myosin II in early syncytial Drosophila embryos: its role in nuclear axial expansion and its regulation by Cdc2 activity. *The Journal of cell biology*, 158(1), pp.127–137.

Stewart, M.P. et al., 2013. Wedged AFM-cantilevers for parallel plate cell mechanics. *Methods*, 60(2), pp.186–194.

Yu, F. et al., 2000. Analysis of partner of inscuteable, a Novel Player of Drosophila Asymmetric Divisions, Reveals Two Distinct Steps in Inscuteable Apical Localization. *Cell*, 100(4), pp.399–409.